

PHISWID: Physics-Inspired Underwater Image Dataset Synthesized from RGB-D Images

Reina Kaneko, *Student Member, IEEE*, Takumi Ueda, Hiroshi Higashi, *Member, IEEE*, and Yuichi Tanaka, *Senior Member, IEEE*

Abstract—This paper introduces the physics-inspired synthesized underwater image dataset (PHISWID), a dataset tailored for enhancing underwater image processing through physics-inspired image synthesis. For underwater image enhancement, data-driven approaches (e.g., deep neural networks) typically demand extensive datasets, yet acquiring paired clean atmospheric images and degraded underwater images poses significant challenges. Existing datasets have limited contributions to image enhancement due to lack of physics models, publicity, and ground-truth atmospheric images. PHISWID addresses these issues by offering a set of paired atmospheric and underwater images. Specifically, underwater images are synthetically degraded by color degradation and marine snow artifacts from atmospheric RGB-D images. It is enabled based on a physics-based underwater image observation model. Our synthetic approach generates a large quantity of the pairs, enabling effective training of deep neural networks and objective image quality assessment. Through benchmark experiments with some datasets and image enhancement methods, we validate that our dataset can improve the image enhancement performance. Our dataset, which is publicly available, contributes to the development in underwater image processing.

Index Terms—underwater image enhancement, marine snow, creating dataset, deep learning.

I. INTRODUCTION

Image restoration and enhancement [1]–[7] has been a long-studied topic for decades, with substantial advancements in the deep learning era. This progress is largely due to the availability of extensive datasets comprising pairs of ground-truth and degraded images. However, the situation changes dramatically when dealing with extreme image restoration scenarios, including underwater, satellite, and medical imaging [8]–[22]. These contexts present atypical degradation patterns that diverge from conventional Gaussian models, and they suffer from a scarcity of training images for algorithm refinement, particularly for deep neural networks.

Underwater image enhancement is one of the extreme image restoration challenges. In underwater, light (especially their red components) is strongly absorbed and scattered, rather than that in atmospheric scenes. This is due to two “depths” in underwater scenes: 1) horizontal distances between the camera and scene (this is the typical “depth” in regular image processing) and 2) water depth. Both of them affect light

absorption and scattering properties, which result in shifting the color of images in underwater [23]. Images are also degraded due to *marine snow* [24], whose artifacts are visible as white dots due to light reflecting off particles like organic matter and sand. Its example is shown in Fig. 1. As a result, underwater image degradation is significantly different from atmospheric images, which results in requirements for image enhancement methods designed for underwater scene.

Many underwater image enhancement methods, both model- and deep learning-based ones, have been proposed [10], [25]–[31]. While their building blocks vary, most works aim to the same goal—producing *clean underwater images*. They may be enough for entertainment purposes, however, in many situations like rescue, defense, bioprospecting/resource exploration, we often need *enhanced underwater images looks like atmospheric images*. For example, we can use an object detection system designed for regular atmospheric images as is when underwater images are restored like atmospheric ones. Fig. 2 shows an example of object detection for a real underwater image and enhanced ones. We simply use a YOLOv5 pretrained model [32] for the object detection experiment. As can be seen, a person cannot be detected with the original underwater image. All of the enhanced images help to detect the person, but the confidence scores are different: Reducing blueish color shift will contribute the accurate detection.

The primary hurdle for underwater image enhancement, especially for yielding atmospheric-like images, lies in the absence of ground-truth images. Unlike regular image processing, obtaining clean atmospheric counterparts for underwater images is not feasible. The lack of pairs of ground-truth and degraded images hampers neural network training, as traditional loss functions (e.g., peak signal to noise ratio (PSNR) and structural similarity (SSIM)) evaluate the error between these pairs [33].

Various underwater image datasets and enhancement methods have tackled to address this lack of ground-truth images [11], [13], [14], [34]–[38]. However, we face the following three problems:

- i) Many datasets are not publicly available [12], [35], [39].
- ii) They often produce clean images as *reverse engineering*: Ground-truth images are obtained by (manual or automatic) enhancement of underwater images. This process does not take into account the above-mentioned two “depths” information in underwater since it is not accompanied with the images. Moreover, enhanced underwater images, i.e., cleaned underwater images, are used as ground-truth [10], [26], [40].

Reina Kaneko, Hiroshi Higashi, and Yuichi Tanaka are with the Graduate School of Engineering, The University of Osaka, Suita, Osaka 565–0861, Japan (e-mail: r.kaneko@sip.comm.eng.osaka-u.ac.jp; higashi@comm.eng.osaka-u.ac.jp; ytanaka@comm.eng.osaka-u.ac.jp).

Takumi Ueda was with the Graduate School of BASE, Tokyo University of Agriculture and Technology, Koganei 184–8588, Japan.

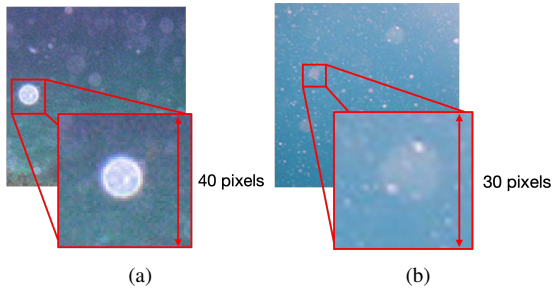


Fig. 1: Marine snow artifacts in real underwater images.

- iii) Many methods overlook a critical aspect of marine snow. This phenomenon degrades overall image quality, yet its removal techniques are often limited to classical median-filtering approaches [41]–[43].

To tackle the above-mentioned challenges, this paper propose a new dataset, the physics-inspired synthesized underwater image dataset (PHISWID), providing pairs of *real atmospheric ground-truth images* and synthesized underwater images with color degradation and marine snow artifacts taking into account the two-depths information [44], [45]. Our dataset is based on physical observation models which enable to synthesis underwater image from real-world RGB-D images. For the physical observation models, the light absorption and scattering model in underwater is used to model color shift [23], [46] and the light scattering model for underwater particle to marine snow [47]. We apply these models to an atmospheric RGB-D image to generate its synthetic underwater image, obtaining a pair of the ground-truth and underwater images.

Our dataset is validated with various image enhancement methods and some existing datasets. We show that the learning-based methods trained with our dataset outperforms the ones trained with the other datasets [10], [26], even with basic Transformer [48]. Our benchmark results suggest a potential contribution of our dataset, which is made publicly available, to development of the underwater image processing¹.

The preliminary version of this paper was presented in [11]. This paper extends it by 1) incorporating marine snow artifacts with physics-based observation models in the dataset, 2) improving the image synthesis process and enhancing resolutions, and 3) providing comprehensive comparisons with alternative datasets and restoration methods.

The remainder of this paper is organized as follows: Section II reviews related studies for underwater image enhancement. We propose underwater image synthesis methods along with the marine snow observation model and the color shift model in Section III. The PHISWID specifications are introduced in Section IV. The benchmarking results with PHISWID are shown in Section V. Real-world examples and limitations are described in Section VI. Finally, we provide some concluding remarks in Section VII.

¹<https://github.com/reina0112/PHISMID-PHISWID>.

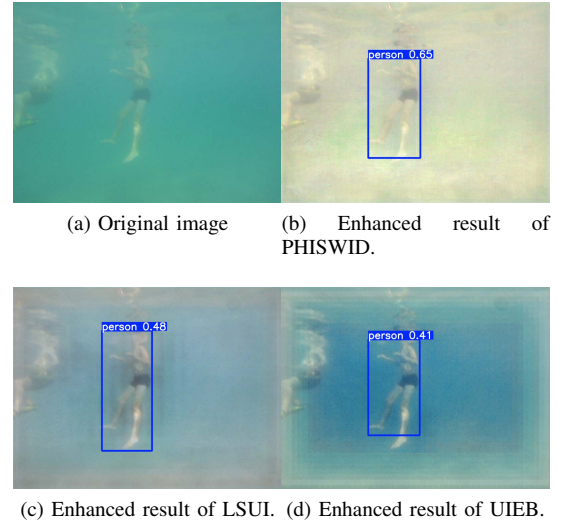


Fig. 2: Object detection results of a test image in the EUVP dataset [31]. We use a YOLOv5 pretrained model [32] for the object detection experiment. The blue squares are estimated bounding boxes and the numbers are confidence score ($[0, 1]$). (a) original image (an object is not detected). (b) enhanced image based on PHISWID. (c) enhanced image based on LSUI. (d) enhanced image based on UIEB. The enhancement method is the same as that in the experiment in Section V.

II. RELATED WORK

In this section, we introduce previous works on underwater image enhancement. We first introduce underwater image enhancement and available datasets, then focus on marine snow removal. Currently available datasets are listed in Table I.

A. Underwater Image Enhancement and Available Datasets

The current trend of underwater image enhancement is based on deep learning as with the other image enhancement/restoration tasks [10], [25]–[28]. In [25], a wavelength-attributed deep neural network is proposed. In [26], a transformer designed for underwater image enhancement is presented. A color correction module followed by an optical model is used in [10], [38]. These methods were trained with datasets including pairs of ground-truth (clean) and underwater (degraded) images for underwater image enhancement. However, collecting extensive pairs in underwater situations is still a challenge. This limits the performance of deep learning-based techniques.

An approach for creating the image pairs is that a clean (ground-truth-like) image is selected among images processed by various enhancement methods by human voting. We call it *voting-based approach*. UIEB dataset [10], which is widely utilized for developing many enhancement methods [10], [25], provides 860 real-world underwater images and corresponding ground-truth-like images across various water conditions. LSUI dataset [26] is also widely used [26], [29]. It contains 4279 real-world underwater images and the corresponding reference images. SAUD dataset [40] contains 100 raw underwater images and enhanced images used some existing

TABLE I: List of underwater image datasets.

Dataset	Target	Number of Images	Method	Availability
PHISWID (proposed)	Color shift & Marine snow	4195	Physics-based synthesis	✓
Dataset used in [35]	Color shift & Haze	10143	Physics-based synthesis & Filtering	
UIEB [10]	Color shift	860	Voting	✓
LSUI [26]	Color shift	4279	Voting	✓
SAUD [40]	Color shift	100	Voting	✓
EUVP [31]	Color shift	12000	Cycle GAN	✓
Dataset used in [12]	Color shift	200	Physics-based synthesis	
Dataset used in [39]	Color shift	1449	Physics-based synthesis	
MSRB [24]	Marine snow	2700	Observation-based synthesis	✓

methods. In the voting-based datasets, there is a possibility that no enhancement method works well on a certain underwater image. Therefore, they do not guarantee that the clean image is close to the *true* ground-truth image which is taken under the atmospheric environment. This gap in the ground-truth images could ruin the reliability of the datasets and lead to limited performance.

Generative adversarial network (GAN)-based approach [14], [30], [31], [49] is also used to generate clean, ground-truth-like images. The GANs are trained with sets of clean and degraded underwater images. A critical limitation of this approach, which does not provide pairs of ground-truth and degraded images, is that well-known full-reference image quality metrics like PSNR and SSIM cannot be computed to evaluate the enhancement/restoration accuracy. Moreover, many datasets are not publicly available and their contribution to image restoration development is limited. Furthermore, there is no dataset including both marine snow artifacts and color shift degradation.

Unlike the voting-based and GAN-based approaches, which generate the ground-truth-like images from underwater images, there is an approach to generate underwater images from ground-truth images which are taken under the atmospheric environment. We call it *physics-based synthesis approach*. In this approach, degraded underwater images are generated from atmospheric images by simulating the degradation processes of absorption and scattering [11], [12], [35], [39]. This approach requires precise models of degradation. However, some datasets [12], [39] are based on oversimplified color degradation processes. They ignore the light scattering and the radiance ratio of the scene reaching the camera. This synthesis may be incomplete for underwater image enhancement purposes. Furthermore, they are not available online (see Table I). It leads to a limited contribution.

B. Marine Snow Removal

Marine snow is one of the main sources of underwater image degradation but has been underaddressed so far. Here, we briefly review some existing marine snow removal approaches.

A widely used method for marine snow removal is a median filter (MF) [41], [50]–[52]. If marine snow artifacts are assumed sufficiently small (typically 1–3 pixels in diameter), MF works well since small marine snow artifacts are similar to salt-and-pepper noise. However, as shown in Fig. 1, marine snow artifacts often become large. As we set a large filter size for MF to remove such artifacts, MF significantly blurs the entire image.

TABLE II: Ten Water types by Jerlov [23].

Ocean water type	Coastal water type
I, IA, IB, II, III	1C, 3C, 5C, 7C, 9C

Low attenuation ← → High attenuation

So far, a few deep learning-based marine snow removal methods have been proposed [24], [36], [53]. A typical training dataset consists of underwater images and their corresponding version with synthesized marine snow artifacts. In [36], marine snow particles are manually appended to underwater images with Adobe Photoshop. This results in a lack of randomness and scalability. In [24], shapes of synthesized marine snow artifacts in the dataset are modeled with ellipses. However, this marine snow synthesis is not based on a physical measurement model of a particle in underwater and the reproduction accuracy of marine snow is limited.

As a result, for underwater image enhancement, we need a dataset including the following images:

- Ground-truth clean atmospheric images, i.e., target images.
- Underwater images corresponding to the atmospheric images degraded by absorption, scattering, and marine snow.

Creating such a dataset by taking many pictures in the real world in various water types is infeasible. Hence, we address this problem by synthesizing images based on physics-guided models for color shift and marine snow.

III. UNDERWATER IMAGE SYNTHESIS

In this section, we describe our method for generating underwater images from clean RGB-D atmospheric images by synthesizing degradation caused by absorption, scattering, and marine snow.

The flow for image synthesis is illustrated in Fig. 3. We first synthesize color-shifted images based on a physics-inspired color shift model proposed in Section III-A through the procedure described in Section III-B. Then, we also synthesize marine snow artifacts based on a model proposed in Section III-C through the procedure described in Section III-D.

A. Color Shift Model

Here, we first describe the models simulating color shift of underwater images.

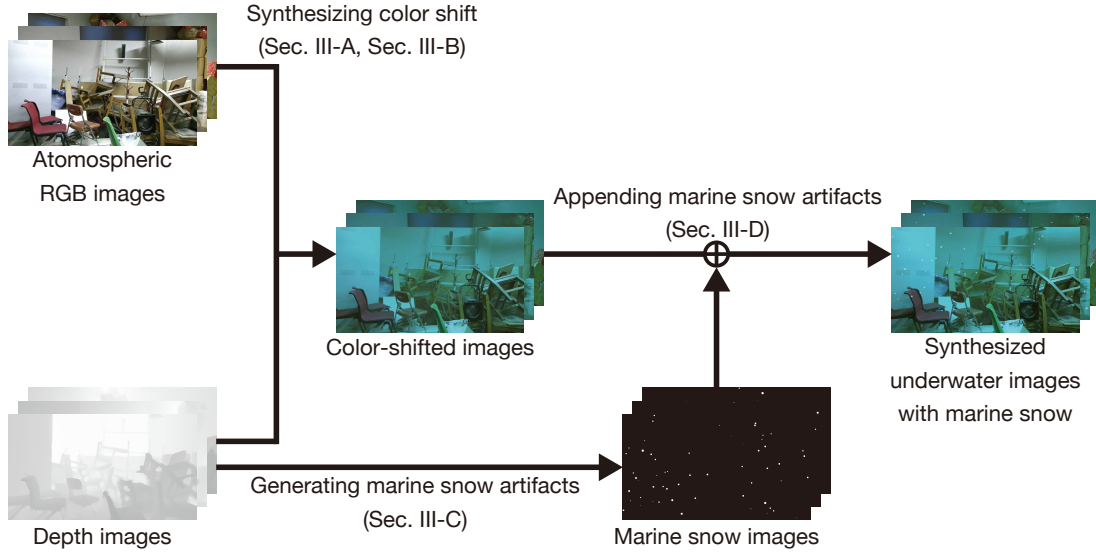


Fig. 3: Flow of underwater image synthesis for PHISWID. First, RGB and depth images are used to synthesize underwater images based on [11]. Then, marine snow artifacts are added with the method introduced in Section III.

Algorithm 1 Color shift synthesis algorithm

Input: Clean RGB-D images : $D_{\text{RGB-D}}$
 Attenuation coefficients for each water type w : $D_{w,\beta(\lambda)}$
 Camera spectral response : $D_{\text{SR}(\lambda),\text{camera}}$
 Illumination irradiance on the water surface : $\Theta_0(\lambda)$
 $d_{\text{vert,max}}, B_{c,\text{min}}, B_{c,\text{max}}, \rho(\lambda) = 1$

Output: Synthesized image set corresponding : $D_{\mathcal{W},\text{synthesized}}$

- 1: $\mathcal{W} \leftarrow \{\text{I, IA, IB, II, III, 1C, 3C}\}$
- 2: **for** $t = 1$ to 7 **do**
- 3: $\beta(\lambda) \leftarrow D_{\mathcal{W}_t,\beta(\lambda)}$
- 4: **repeat**
- 5: $\Phi \leftarrow$ Clean image in $D_{\text{RGB-D}}$
- 6: $z \leftarrow$ Depth map in $D_{\text{RGB-D}}$
- 7: Adjust the dynamic range of D_h into $d_{\text{horiz}} \in [0.5, 14]$
- 8: Set d_{vert} within $0.5 \leq d_{\text{vert}} \leq d_{\text{vert,max}}$ randomly
- 9: Set B_c within $B_{c,\text{min}} \leq B_c \leq B_{c,\text{max}}$ randomly
- 10: Randomly select a camera r
- 11: $\text{SR}(\lambda) \leftarrow D_{\text{SR}(\lambda),r}$
- 12: Calculate equation (1)–(5) for all pixels and get U_c
- 13: Put U_c into $D_{\mathcal{W}_t,\text{synthesized}}$
- 14: **until** Generating U_c from all images in $D_{\text{RGB-D}}$
- 15: **end for**

1) *Algorithm Overview:* Our color shift model considers attenuation of light due to underwater condition and spectral difference of camera property. For modeling the attenuation, we use a model proposed by Jerlov [23] which presents attenuation of light at each wavelength (400 to 700 nm). The attenuation coefficients are varied for water types, which Jerlov classified into ten as shown in Table II. We omit three coastal water types, 5C, 7C, and 9C, from our dataset because objects are almost invisible for these types. In addition to the attenuation property, the color also depends on the spectrum response which is an inherent property of a camera and lens.

Therefore, our color shift synthesis takes into account the attenuation and spectral response to simulate the color shift in underwater environment.

Algorithm 1 describes the overview of our color shift synthesis method. The required inputs are listed as follows:

- Clean RGB-D images: $D_{\text{RGB-D}}$.
- Set of attenuation coefficients $\beta(\lambda)$ for each water type w , in which λ is the wavelength: $D_{w,\beta(\lambda)}$.
- Set of RGB spectral responses SR(λ) for several digital cameras: $D_{\text{SR}(\lambda),\text{camera}}$.
- Illumination irradiance on the water surface: $\Theta_0(\lambda)$.
- Maximum vertical distance from water surface²: $d_{\text{vert,max}}$
- Maximum and minimum values of the background light: $B_{c,\text{max}}$ and $B_{c,\text{min}}$.

Our algorithm creates seven sets of synthetic images, each corresponds to one water type.

2) *Underwater Image Degradation Model:* In our color shift model, we consider two main sources of the degradation process: absorption and scattering. The underwater color shift model is represented as follows:

$$U_c(x, y) = T_{c,d_{\text{vert}}} T_{c,d_{\text{horiz}}} \Phi(x, y) + B_c T_{c,d_{\text{vert}}} (1 - T_{c,d_{\text{horiz}}}), \quad (1)$$

where $c \in \{\text{R, G, B}\}$, $U_c(x, y)$ is the pixel values at (x, y) of an underwater image, $\Phi(x, y)$ is the pixel values of the corresponding clean RGB-D image, $T_{c,d_{\text{vert}}}$ is the transmission map of color at the vertical distance d_{vert} , and $T_{c,d_{\text{horiz}}}$ is that in the horizontal direction (i.e., the distance between the camera and scene).

The first term in (1) represents the process of color absorption both in the vertical and the horizontal directions. The second term corresponds to the background color at the

²In this paper, we do not use “depth” for water depth not to confuse readers.

vertical distance d_{vert} and the horizontal distance d_{horiz} . Further, $T_{c,d_{\text{vert}}}$ and $T_{c,d_{\text{horiz}}}$ is obtained by

$$T_{c,d_{\text{vert}}} = \exp(-\beta_{c,d_{\text{vert}}} \cdot d_{\text{vert}}) \quad (2)$$

$$T_{c,d_{\text{horiz}}} = \exp(-\beta_{c,d_{\text{horiz}}} \cdot d_{\text{horiz}}), \quad (3)$$

where $\beta_{c,d_{\text{vert}}}$ and $\beta_{c,d_{\text{horiz}}}$ are the attenuation coefficients along the vertical and horizontal directions, respectively.

Based on [46], $\beta_{c,d}$ and $\beta_{c,d_{\text{horiz}}}$ is given as

$$\beta_{c,d_{\text{vert}}} = d_{\text{vert}}^{-1} \ln \left[\frac{\int \text{SR}(\lambda) \rho(\lambda) \Theta_0(\lambda) d\lambda}{\int \text{SR}(\lambda) \rho(\lambda) \Theta_0(\lambda) \exp[-\beta(\lambda) d_{\text{vert}}] d\lambda} \right] \quad (4)$$

$$\beta_{c,d_{\text{horiz}}} = \frac{\ln \left[\frac{\int \text{SR}(\lambda) \rho(\lambda) \Theta_0(\lambda) \exp[-\beta(\lambda) d_{\text{vert}}] d\lambda}{\int \text{SR}(\lambda) \rho(\lambda) \Theta_0(\lambda) \exp[-\beta(\lambda) (d_{\text{vert}} + d_{\text{horiz}})] d\lambda} \right]}{d_{\text{horiz}}}, \quad (5)$$

where $\rho(\lambda)$ is the reflectance spectrum of the object surface. By using (4) and (5), we obtain attenuation coefficients to calculate $T_{c,d_{\text{vert}}}$ and $T_{c,d_{\text{horiz}}}$.

B. Synthesizing Color Shift

By using the models introduced in Section III-A, we synthesize the color shift. We use the attenuation coefficients in all frequency ranges in contrast to the existing work [39] using only three coefficients.

The attenuation coefficients for seven water types $D_{w,\beta(\lambda)}$ (see Algorithm 1), are given by [54]. We also use the data of solar irradiance on the water surface [55] as $\Theta_0(\lambda)$. The camera spectrum responses are also given from the dataset of 28 digital cameras [56]. The other parameters are set to $d_{\text{vert,max}} = 1$, $\{B_{R,\text{min}}, B_{G,\text{min}}, B_{B,\text{min}}\} = \{0.4, 0.7, 0.7\}$, and $\{B_{R,\text{max}}, B_{G,\text{max}}, B_{B,\text{max}}\} = \{0.5, 0.8, 0.8\}$ [11]. We randomly determine one of B_c and d_{vert} from the uniform distribution in the range of $B_{c,\text{min}} \leq B_c \leq B_{c,\text{max}}$ and $0.5 \leq d_{\text{vert}} \leq d_{\text{vert,max}}$, respectively. As a result, 7 underwater images are generated from a single atmospheric image with the seven water types and the one set of B_c and d_{vert} .

C. Marine Snow Model

1) *Light Scattering of Marine Snow*: Although a precise model of marine snow artifacts requires to identify particles, the identification is impractical since any particle drifting in underwater could be the sources. Therefore, we consider light scattering in water for small particles based on the Jaffe-MacGlamery model [47], [57], which is common for underwater imagery [49], [58].

The Jaffe-MacGlamery model of a small object is illustrated in Fig. 4(a). The model considers direct-scattered and back-scattering components [47], [57]. Although the back-scattering components should be considered if a object is relatively large, we can ignore these components because objects caused marine snow should be small. Therefore, we simplify the model only with the direct-scattered components. Another simplification is that there is a single light source in a scene. We assume that a camera's flash is the single source. The model with these two simplifications is illustrated in Fig. 4(b).

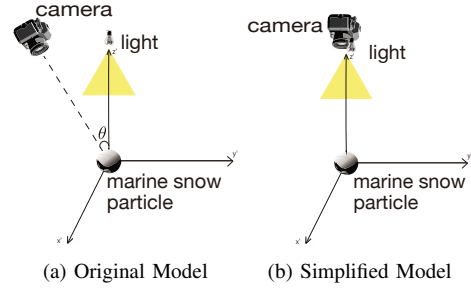


Fig. 4: Jaffe-MacGlamery model.

TABLE III: Parameter settings for light scattering in (6) and (8).

Parameter	Setting
θ	0
$E_d(x, y)$	Direct-scattered component
F_l	Focal length of camera
T_l	Transmittance of the lens
R	Distance from camera to marine snow
β_c	Attenuation along the vertical and horizontal directions
$p(\cdot)$	Point spread function

The direct-scattered component $E_d(x, y)$ at the coordinate (x, y) in the observed image is thus represented as

$$E_d(x, y) = E_1(x, y, 0) e^{-\beta_c R} M(x, y) \frac{\cos^4 \theta T_l}{4f_n} \left[\frac{R - F_l}{R} \right]^2, \quad (6)$$

where $E_1(x, y, 0)$ is defined as

$$E_1(x, y, 0) = E_1'(x, y, 0) * p(x, y | R, G, \beta_c, B) + E_1''(x, y, 0), \quad (7)$$

and $*$ is convolution, $M(x, y)$ is the reflectance values of the reflectance map for oceanographic objects. The other symbols are defined in Table III.

Here, we further assume the light source and the camera are located in the same 3D position, which results in $\theta = 0$. This simplifies the observation model as in Fig. 4(b). By the above assumption, (6) can be rewritten as

$$E_d(x, y) = \left(A \frac{e^{-2\beta_c R}}{R^2} * p + A \frac{e^{-2\beta_c R}}{R^2} \right) \left[\frac{R - F_l}{R} \right]^2, \quad (8)$$

where A is a constant coming from those in (6). The simplified model in (8) indicates that the light scattering of a marine snow particle only depends on R , i.e., the distance between the camera and the particle. The derivation of the equation is shown in Appendix A.

2) *Modeling Marine Snow Artifacts*: Based on the observation model shown in Section III-C1, we model the type H and V³ marine snow artifacts. The type H artifacts correspond to generic marine snow particles. The type V artifacts are often observed as an edge-enhanced version of the type H caused by automatic image processing in cameras (like those in smartphones). An example of type H and V marine snow is shown in Fig. 5.

³“H” and “V” refer to “highland” and “volcanic crater”, respectively, as in [24].

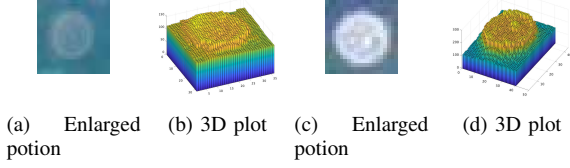


Fig. 5: Marine snow examples in real underwater images. Left: Type H. Right: Type V.

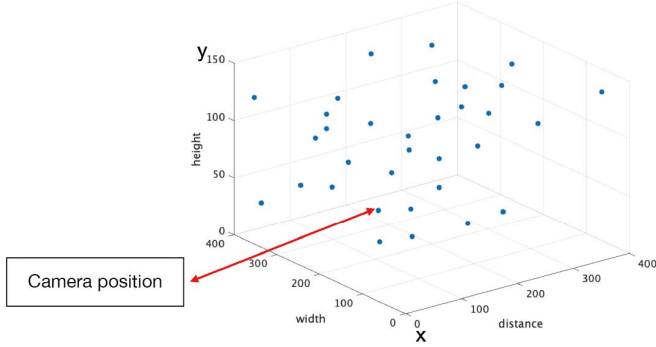


Fig. 6: Illustrative example of marine snow particles. Particles are synthesized at the blue dot locations.

We model a type H marine snow artifact as a Gaussian filtered version of a point source according to (8). The type V is the slightly modified version of the type H. Since the luminance of a particle depends on R , i.e., the distance between the camera and the particle, we model marine snow particles with the following steps:

- i) **Particle Setting:** As shown in Fig. 6, suppose that the camera is positioned parallel to the (x, y) -plane and at a sufficiently large distance from the scene located in the three-dimensional Euclidean space. The three-dimensional coordinates of the particles are uniformly set. The number of marine snow particles is given for each image.

A sparse matrix $\tilde{S} \in \mathbb{R}^{H \times W}$ for the particle coordinates, where H and W are the height and width of the target image, is created as

$$\tilde{S}(x, y) = \begin{cases} R & \text{if a particle is located at } (x, y) \\ 0 & \text{otherwise,} \end{cases} \quad (9)$$

where R is randomly set.

We then make a set of matrices $\{E_n\}_n$ such that $\tilde{S} = \sum_{n=0}^{N-1} E_n$ based on \tilde{S} as follows:

$$E_n(x, y) = \begin{cases} D & \text{if } d_{\text{horiz}, n-1} < \tilde{S}(x, y) \leq d_{\text{horiz}, n} \\ 0 & \text{otherwise,} \end{cases} \quad (10)$$

where D is a constant corresponding to the brightness of a particle and $d_{\text{horiz}, n}$ is the pre-determined horizontal distance from the camera where $d_{\text{horiz}, -1} = 0$. This helps to reduce the computational cost for the following Gaussian filtering.

- ii) **Gaussian filtering to particles:** Let $g(x, y; \sigma_n)$ be a Gaussian filter centered at (x, y) with the parameter σ_n . We apply $g(x, y; \sigma_n)$ to E_n for yielding S_n for the prototype of the marine snow artifacts.

$$S_n(x, y) = g(x, y; \sigma_n) * E_n(x, y). \quad (11)$$

- iii) **Thresholding:** To avoid overshooting of the luminance of marine snow artifacts, thresholding is performed as

$$H_n(x, y) = \begin{cases} a_n S_n(x, y) & S_n(x, y) < \text{threshold} \\ \text{constant} & S_n(x, y) \geq \text{threshold,} \end{cases} \quad (12)$$

where a_n is a pre-determined constant to strengthen or weaken the luminance of the artifacts.

Finally, an image only containing marine snow artifacts is obtained by $H = \sum_n H_n$. The synthesized type H marine snow artifact is shown in Figs. 7(a) and (b), which are similar to the real version in Figs. 5(a) and (b).

We model the type V artifacts by applying the Laplacian filter to the type H artifacts. For type V, steps i) and ii) are the same as type H. Step iii) is different as:

- iii') **Laplacian filtering and thresholding:**

$$V_n(x, y) = \begin{cases} L(\sigma_n) * a'_n S'_n(x, y) & V < \text{threshold} \\ \text{constant} & V \geq \text{threshold,} \end{cases} \quad (13)$$

where $L(\sigma_n)$ is a Laplacian filter for edge enhancement with the parameter σ_n controlling sharpness and a'_n is similar to a_n in (12).

Finally, an image only containing marine snow artifacts is obtained by $V = \sum_n V_n$. The synthesized type V marine snow artifact is shown in Figs. 7(c) and (d). Like the type H, it is also similar to the artifacts in the real-world image in Figs. 5(c) and (d).

D. Synthesizing Marine Snow Artifacts

By using the models introduced in Section III-C, we synthesize the marine snow artifacts with underwater images or synthesized underwater images.

Let $U_c \in \mathbb{R}^{H \times W \times 3}$ be an underwater image obtained by the model introduced in Section III-A. To synthesize marine snow artifacts, we simply overlay $H(x, y)$ and $V(x, y)$ on $U_c(x, y)$ as:

$$I_c(x, y) = U_c(x, y) + H(x, y) + V(x, y), \quad (14)$$

where $H(x, y)$ and $V(x, y)$ are images with the type H and V marine snow artifacts shown in (12) and (13), respectively.

IV. PHISWID SPECIFICATIONS

Our developed dataset, PHISWID, contains 4195 image pairs, all having a pixel resolution of 1344×756 . All original atmospheric RGB-D images used are collected from the large-scale RGB-D database [59]–[63]. An image pair contains one original atmospheric image and one synthesized underwater image degraded by color shift and marine snow artifacts. We randomly set water type for each image. Image examples in PHISWID are shown in Fig. 8.

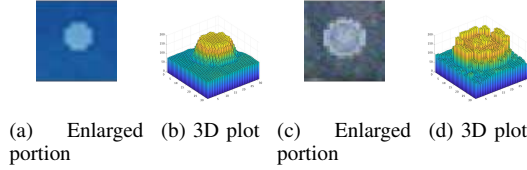


Fig. 7: Synthesized marine snow artifact examples. Left: Type H. Right: Type V.



Original images.



Synthesized images.

Fig. 8: Example images in PHISWID.

Each synthesized image contains marine snow artifacts. The number of the type H marine snow particles is randomly generated with a Gaussian distribution of mean 40 and variance 5, and that of the type V marine snow particles conforms to a Gaussian distribution of mean 30 and variance 5.

Most parameters are determined according to our preliminary observations of real underwater images: They are summarized in Appendix B.

V. BENCHMARKING RESULTS ON SYNTHESIZED IMAGES

In this section, we compare three datasets (PHISWID, UIEB, and LSUI) using the same module to demonstrate the contribution of our dataset to underwater image enhancement. In addition, we compare other modules using different datasets.

A. Setup

We divided PHISWID to 4125 training image pairs and 70 test image pairs. Underwater image enhancement performance is compared with various methods summarized in

TABLE IV: Comparison methods.

Abbreviation	Baseline module	Training dataset
Trans(P)	Transformer	PHISWID
Trans(P')	Transformer	PHISWID w/o marine snow
DWN(P)	Deep WaveNet	PHISWID
Trans(U)	Transformer	UIEB
DWN(U) [25]	Deep WaveNet	UIEB
WN [10]	WaterNet	UIEB
Trans(L)	Transformer	LSUI
U-shape [26]	Transformer	LSUI
HLRP [38]	Model-based enhancement	-

TABLE V: Average PSNRs and SSIMs over the test dataset of PHISWID.

Method	PSNR \uparrow	SSIM \uparrow	NIQE \downarrow
Trans(P)	21.00	0.793	2.86
Trans(P')	19.10	0.748	3.69
DWN(P)	21.10	0.671	3.11
Trans(U)	14.69	0.286	4.13
DWN(U)	16.60	0.359	3.67
WN	17.06	0.359	3.76
Trans(L)	15.06	0.363	4.05
U-shape	14.88	0.368	3.11
HLRP	7.10	0.062	NaN
Synthesized image	13.67	0.120	4.02

Table IV. The parameters of the alternative methods are basically followed to the original researches. We use WaterNet (abbreviated as WN) [10], Deep WaveNet (abbreviated as DWN) [25], U-shape Transformer (abbreviated as U-shape) [26] and HLRP [38], which are widely used for underwater image enhancement and restoration. WN, DWN(U), and U-shape are trained with their own datasets.

To compare dataset qualities, we trained DWN with the proposed PHISWID. Furthermore, we train Transformers with PHISWID (abbreviated as Trans(P)), UIEB (abbreviated as Trans(U)) [10], and LSUI (abbreviated as Trans(L)) [26]. The structure of the Transformer is shown in Appendix C. For a comparison purpose, we also train the same Transformer with the dataset *without* marine snow artifacts, i.e., the dataset only applied our color shift model (abbreviated as Trans(P')).

For objective quality comparison, we compute the average PSNRs and SSIMs over the test datasets. We also show naturalness image quality evaluator (NIQE) [64] as a non-reference quality metric. NIQE fits our purpose of the paper because it returns a low score when images are *natural taken in atmospheric scenes*.

B. Results

The experimental results are shown in Fig. 9 and the objective performances are summarized in Table V. All of the metrics (PSNRs, SSIMs, and NIQEs) of the neural networks trained with PHISWID outperform those with the existing datasets. Fig. 9 visualizes such differences: The methods trained with PHISWID restore images like their atmospheric counterparts. On the other hand, marine snow artifacts remain and blueish images are still generated by methods trained with the alternative datasets. Trans(P') can remove blueish color shift, however, it cannot remove marine snow artifacts.

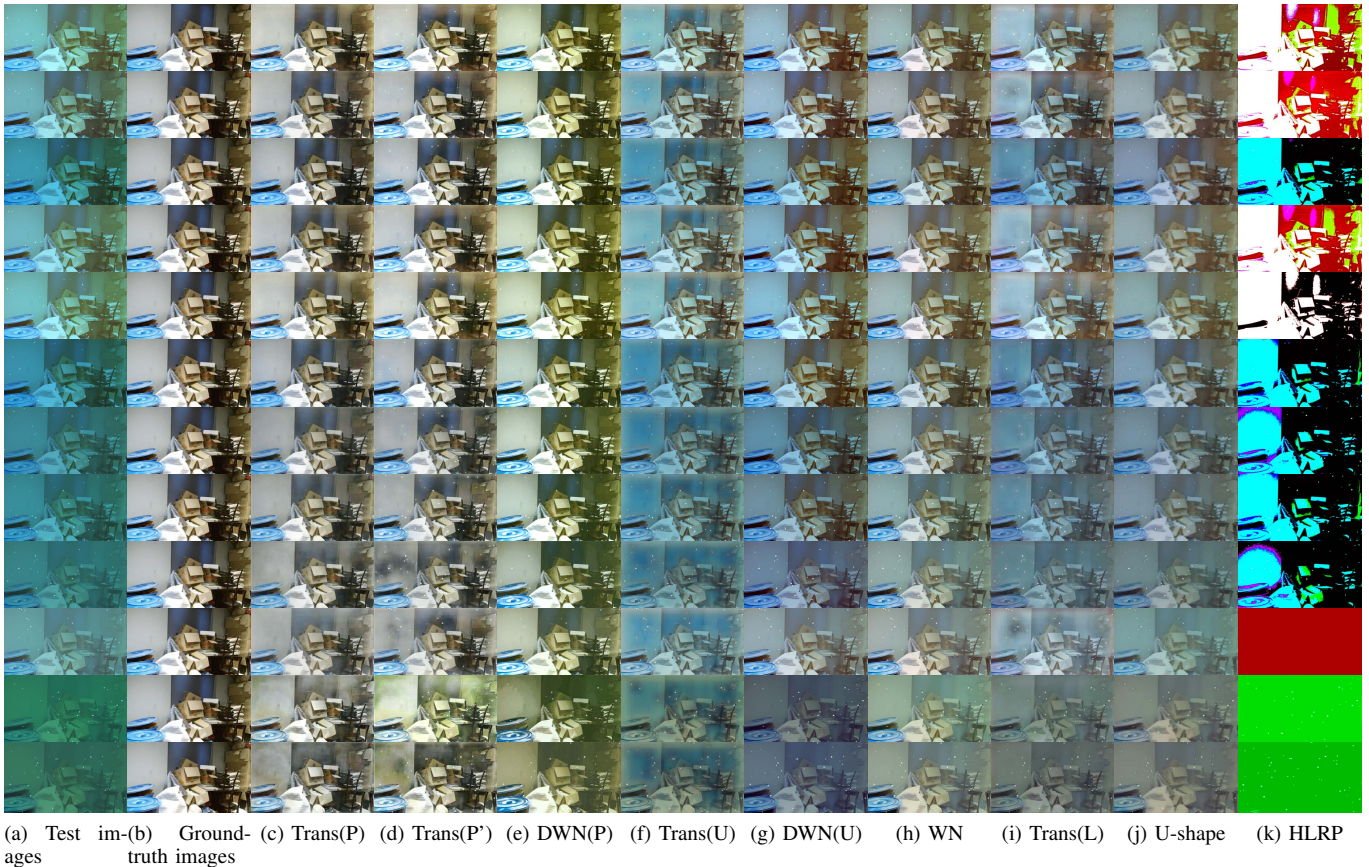


Fig. 9: Image enhancement results with PHISWID test images. From up to down, we use different water types

TABLE VI: Average NIQE over real images.

Method	NIQE↓
Trans(P)	4.07
Trans(P')	4.01
DWN(P)	3.88
Trans(U)	4.30
DWN(U)	4.21
WN	4.64
Trans(L)	4.57
U-shape	4.97
HLRP	NaN
Original image	4.62

VI. REAL-WORLD EXAMPLES

In this section, we present image enhancement results by methods trained by PHISWID for real-world underwater images. We also discuss limitations.

A. Real-world Underwater Image Enhancement

We compare the methods used in Section V-A through real-world underwater images.

Fig. 10 shows underwater image enhancement results for real-world images. All original images are collected from flickr⁴ under a Creative Commons AttributionNonCommercial-ShareAlike 2.0 Generic (CC BY-NC-SA 2.0) License. We also show results for image taken

⁴<https://www.flickr.com/>

from the UIEB challenging set [10] in Fig. 11. We calculate the average NIQE of 66 real-world images, including Fig. 10 and UIEB challenging sets, is summarized in Table VI.

As shown in the figures, methods trained with PHISWID remove color shift sufficiently. A significant difference between PHISWID and the other datasets can be observed in background regions. The PHISWID-based methods have a strong effect to remove the bluish color shift in the background.

The PHISWID-based methods also remove marine snow artifacts and small bubbles similar to marine snow artifacts. Fig. 12 shows enlarged portions of the enhancement results. In contrast, Trans(P') and the methods trained with the existing datasets fail to remove the artifacts.

B. Limitations

Although our PHISWID are carefully designed based on physical measurement processes, we still assume many parameters and settings as shown in Table VII: This is one of the limitations.

As observed in Fig. 10, thick marine snow artifacts still remain in the restored images. The reason for this could be two-fold: First, the architectures of the neural networks are not specifically designed for underwater image enhancement with marine snow artifacts. Second, our proposed model classifies marine snow artifacts into two representative types. Our modeling based on this classification could be incomplete

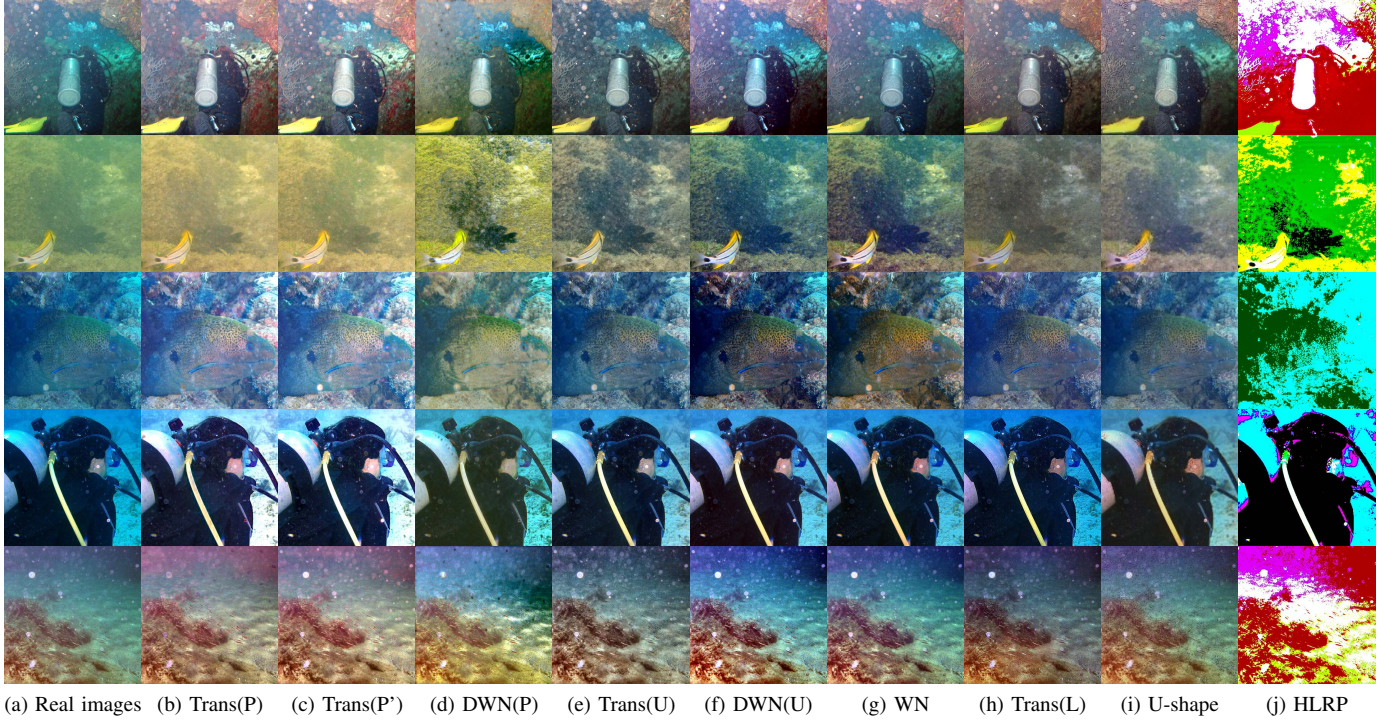


Fig. 10: Underwater image enhancement results for real-world images.

since particles causing marine snow have various structures [65].

Depths beyond our assuming ranges also affect the overall qualities. If the light scattering is very different from the training images, color shift, particularly in the distant backgrounds, could not be well restored as shown in Fig. 13. A possible reason for this low performance is that the RGB-D images used in PHISWID are recorded in indoor situations which results in limited horizontal distances (i.e., depth) in scenes. Therefore it may not appropriately restore color shifts of distant backgrounds.

Our future work includes to update PHISWID for covering broader distance and degradation patterns.

VII. CONCLUSIONS

In this paper, we propose PHISWID for underwater image enhancement. The proposed dataset has a wide variety of underwater image degradation including overlooked effects of marine snow. We physically modeled color shift and marine snow artifacts, and synthesized them in atmospheric RGB-D images. The first benchmarking is performed with PHISWID. The benchmark suggested that methods aided our dataset can improve underwater image enhancement objectively and subjectively.

APPENDIX A

DETAILED DERIVATION OF THE JAFFE-MACGLAMERY MODEL

We describe detailed derivations of the Jaffe-MacGlamery model introduced in Section III-C1.

The following is the original equation in the main paper:

$$E_d(x, y) = E_I(x, y, 0) e^{-\beta_c R} M(x, y) \cdot \frac{\cos^4 \theta T_l}{4f_n} \left[\frac{R - F_l}{R} \right]^2. \quad (15)$$

By substituting angles into (15), the equation is rewritten as:

$$E_d(x, y) = E_I(x, y, 0) e^{-\beta_c R} M(x, y) \cdot \frac{T_l}{4f_n} \left[\frac{R - F_l}{R} \right]^2, \quad (16)$$

where $E_I(x, y, 0)$ is defined as [47]:

$$E_I(x, y, 0) = A' \cos \gamma \frac{e^{-\beta_c R}}{R^2} * p + A' \cos \gamma \frac{e^{-\beta_c R}}{R^2}, \quad (17)$$

where A' is a constant. Substituting (17) into (16), we obtain:

$$E_d(x, y) = (A' \frac{e^{-\beta_c R}}{R^2} * p + A' \frac{e^{-\beta_c R}}{R^2}) e^{-\beta_c R} \times M(x, y) \frac{\cos^4 \theta T_l}{4f_n} \left[\frac{R - F_l}{R} \right]^2, \quad (18)$$

where $M(x, y)$, T_l , and f_n are constant. By merging all the above constant values, we finally obtain the following:

$$E_d(x, y) = (A \frac{e^{-2\beta_c R}}{R^2} * p + A \frac{e^{-2\beta_c R}}{R^2}) \left[\frac{R - F_l}{R} \right]^2. \quad (19)$$

APPENDIX B

PARAMETERS FOR MARINE SNOW MODELS

Table VII summarizes the parameters used for modeling marine snow artifacts.

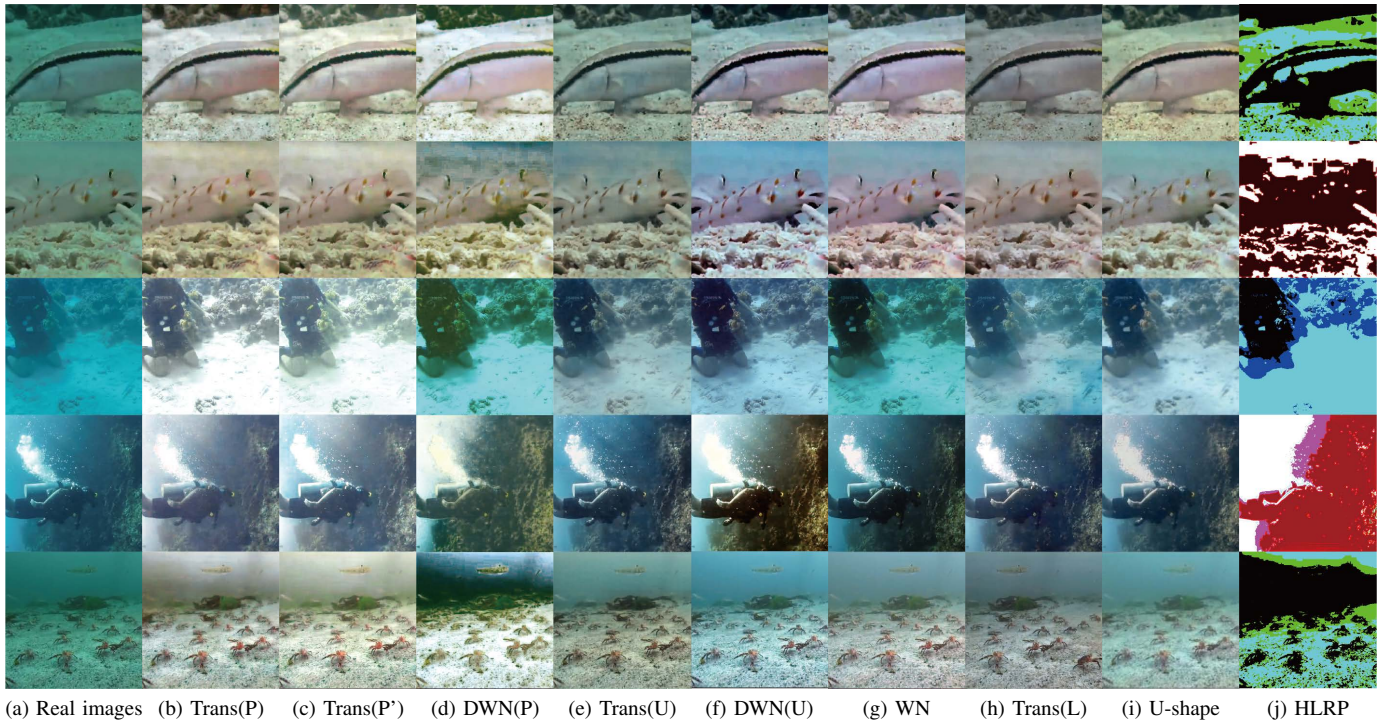


Fig. 11: Underwater image enhancement results for real-world images in UIEB challenges.

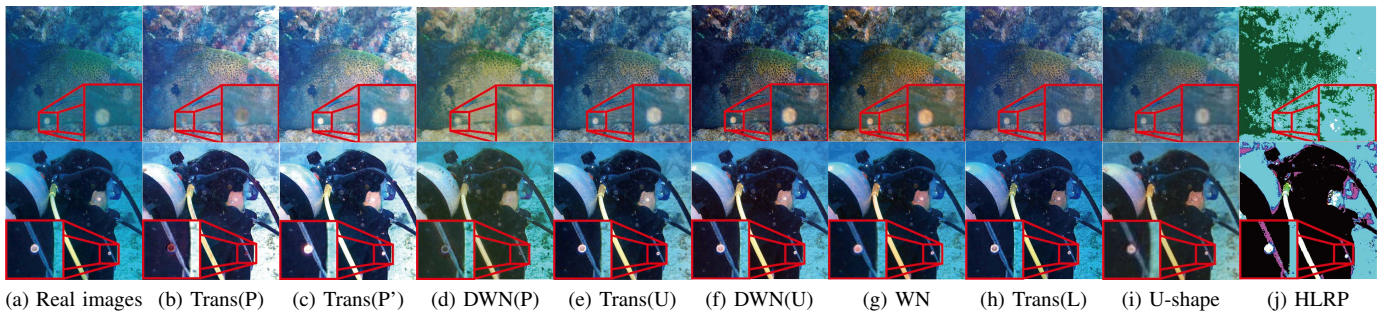


Fig. 12: Enlarged portion of marine snow removal.

APPENDIX C TRANSFORMER STRUCTURE

The structure of Transformer [48] used for our underwater image enhancement experiments in Sections V and VI are illustrated in Fig. 14. The hyperparameters are summarized in Table VIII.

REFERENCES

- [1] K. Zhang, W. Zuo, Y. Chen, D. Meng, and L. Zhang, “Beyond a gaussian denoiser: Residual learning of deep CNN for image denoising,” *IEEE Transactions on Image Processing*, vol. 26, no. 7, pp. 3142–3155, Jul. 2017.
- [2] S. H. Chan, X. Wang, and O. A. Elgendy, “Plug-and-play ADMM for image restoration: Fixed-point convergence and applications,” *IEEE Transactions on Computational Imaging*, vol. 3, no. 1, pp. 84–98, Mar. 2016.
- [3] Y. Romano, M. Elad, and P. Milanfar, “The little engine that could: Regularization by denoising (RED),” *SIAM Journal on Imaging Sciences*, vol. 10, no. 4, pp. 1804–1844, 2017.
- [4] J. Xie, L. Xu, and E. Chen, “Image denoising and inpainting with deep neural networks,” *Advances in neural information processing systems*, vol. 25, pp. 341–349, 2012.
- [5] C. Chen, Z. Xiong, X. Tian, and F. Wu, “Deep boosting for image denoising,” in *Proceedings of the European Conference on Computer Vision (ECCV)*, 2018, pp. 3–18.
- [6] L. Xu, J. S. Ren, C. Liu, and J. Jia, “Deep convolutional neural network for image deconvolution,” in *Advances in neural information processing systems*, vol. 27, 2014, pp. 1790–1798.
- [7] R. A. Yeh, C. Chen, T. Yian Lim, A. G. Schwing, M. Hasegawa-Johnson, and M. N. Do, “Semantic image inpainting with deep generative models,” in *Proceedings of the IEEE/CVF Conference on Computer Vision and Pattern Recognition (CVPR)*, Jul. 2017, pp. 5485–5493.
- [8] D. Akkaynak and T. Treibitz, “A revised underwater image formation model,” in *Proceedings of the IEEE/CVF Conference on Computer Vision and Pattern Recognition (CVPR)*, Jun. 2018, pp. 6723–6732.
- [9] D. Berman, T. Treibitz, and S. Avidan, “Diving into haze-lines: Color restoration of underwater images,” in *Proc. British Machine Vision Conference (BMVC)*, vol. 1, no. 2, 2017, pp. 1–12.
- [10] C. Li, C. Guo, W. Ren, R. Cong, J. Hou, S. Kwong, and D. Tao, “An underwater image enhancement benchmark dataset and beyond,” *IEEE Transactions on Image Processing*, vol. 29, pp. 4376–4389, 2020.
- [11] T. Ueda, K. Yamada, and Y. Tanaka, “Underwater image synthesis from

TABLE VII: Parameter settings for marine snow synthesis.

Type	Parameter	Setting	Corresponding equation or subsection
H	$\{d_{-1,horiz}, d_{0,horiz}, d_{1,horiz}, d_{2,horiz}\}$	{0, 64, 128, 192}	(5)
H	$\{\sigma_1, \sigma_2, \sigma_3, \sigma_4\}$	{7, 5, 3, 3}	Sec. 3.2
H	$\{a_1, a_2, a_3, a_4\}$	{80, 100,150,200}	(6)
H	threshold	80	(6)
V	$\{d_{-1,horiz}, d_{0,horiz}, d_{1,horiz}, d_{2,horiz}\}$	{0, 64, 128, 192}	(5)
V	$\{\sigma_1, \sigma_2, \sigma_3, \sigma_4\}$	{7, 5, 4, 4}	Sec. 3.2
V	σ	0.2	(7)
V	$\{a'_1, a'_2, a'_3, a'_4\}$	{70, 80, 120, 150}	(7)
V	threshold	28	(7)



Fig. 13: Limitations. Top: Original images. Bottom: Restoration results by Trans(P).

TABLE VIII: Parameter settings for Transformer.

Parameter	Setting
Learning rate	0.0001
Number of epochs	60
Initialized bias values	0

RGB-d images and its application to deep underwater image restoration,” in *Proc. 2019 IEEE International Conference on Image Processing (ICIP)*, Sep. 2019, pp. 2115–2119.

- [12] Y. Wang, J. Zhang, Y. Cao, and Z. Wang, “A deep CNN method for underwater image enhancement,” in *2017 IEEE International Conference on Image Processing (ICIP)*, Sep. 2017, pp. 1382–1386.
- [13] C. Li, S. Anwar, and F. Porikli, “Underwater scene prior inspired deep underwater image and video enhancement,” *Pattern Recognition*, vol. 98, p. 107038, 2020.
- [14] Q. Jiang, Y. Chen, G. Wang, and T. Ji, “A novel deep neural network for noise removal from underwater image,” *Signal Processing: Image Communication*, vol. 87, p. 115921, 2020.
- [15] X. Chen, S. Xiang, C.-L. Liu, and C.-H. Pan, “Vehicle detection in satellite images by hybrid deep convolutional neural networks,” *IEEE Geoscience and remote sensing letters*, vol. 11, no. 10, pp. 1797–1801, Oct. 2014.
- [16] L. Zhang, L. Zhang, and B. Du, “Deep learning for remote sensing data: A technical tutorial on the state of the art,” *IEEE Geoscience and Remote Sensing Magazine*, vol. 4, no. 2, pp. 22–40, Jun. 2016.
- [17] X. X. Zhu, D. Tuija, L. Mou, G.-S. Xia, L. Zhang, F. Xu, and F. Fraundorfer, “Deep learning in remote sensing: A comprehensive review and list of resources,” *IEEE Geoscience and Remote Sensing Magazine*, vol. 5, no. 4, pp. 8–36, Dec. 2017.
- [18] E. Maggiori, Y. Tarabalka, G. Charpiat, and P. Alliez, “Convolutional neural networks for large-scale remote-sensing image classification,” *IEEE Transactions on Geoscience and Remote Sensing*, vol. 55, no. 2, pp. 645–657, Feb. 2016.
- [19] D. Shen, G. Wu, and H.-I. Suk, “Deep learning in medical image analysis,” *Annual review of biomedical engineering*, vol. 19, no. 1, pp. 221–248, 2017.
- [20] G. Litjens, T. Kooi, B. E. Bejnordi, A. A. A. Setio, F. Ciompi, M. Ghafoorian, J. A. Van Der Laak, B. Van Ginneken, and C. I. Sánchez, “A survey on deep learning in medical image analysis,” *Medical image analysis*, vol. 42, pp. 60–88, 2017.
- [21] M. Weigert, U. Schmidt, T. Boothe, A. Müller, A. Dibrov, A. Jain, B. Wilhelm, D. Schmidt, C. Broaddus, S. Culley, and others, “Content-aware image restoration: pushing the limits of fluorescence microscopy,” *Nature methods*, vol. 15, no. 12, pp. 1090–1097, Nov. 2018.
- [22] S. Anwar and C. Li, “Diving deeper into underwater image enhancement: A survey,” *Signal Processing: Image Communication*, vol. 89, no. 2, p. 115978, Jan. 2020.
- [23] N. Jerlov, *Optical Classification*. Elsevier, 1968.
- [24] R. Kaneko, Y. Sato, T. Ueda, H. Higashi, and Y. Tanaka, “Marine snow removal benchmarking dataset,” in *2023 Asia Pacific Signal and Information Processing Association Annual Summit and Conference (APSIPA ASC)*, 2023, pp. 771–778.
- [25] P. Sharma, I. Bisht, and A. Sur, “Wavelength-based attributed deep neural network for underwater image restoration,” *ACM Transactions on Multimedia Computing, Communications and Applications*, vol. 19, no. 1, pp. 1–23, Jan. 2023.
- [26] L. Peng, C. Zhu, and L. Bian, “U-shape transformer for underwater image enhancement,” *IEEE Transaction on Image Processing*, vol. 32, pp. 3066–3079, 2023.
- [27] H. Wang, W. Zhang, L. Bai, and P. Ren, “Metalantis: A comprehensive underwater image enhancement framework,” *IEEE Transactions on Geoscience and Remote Sensing*, vol. 62, pp. 1–19, 2024.
- [28] H. F. Tolie, J. Ren, and E. Elyan, “DICAM: Deep inception and channel-wise attention modules for underwater image enhancement,” *Neurocomputing*, vol. 584, p. 127585, Jun. 2024.
- [29] C. Zhao, W. Cai, C. Dong, and C. Hu, “Wavelet-based fourier information diffusion with frequency diffusion adjustment for underwater image restoration,” in *Proceedings of the IEEE/CVF Conference on Computer Vision and Pattern Recognition (CVPR)*, Jun. 2024, pp. 8281–8291.
- [30] C. Fabbri, M. J. Islam, and J. Sattar, “Enhancing underwater imagery using generative adversarial networks,” in *2018 IEEE International Conference on Robotics and Automation (ICRA)*, May 2018, pp. 7159–7165.
- [31] M. J. Islam, Y. Xia, and J. Sattar, “Fast underwater image enhancement for improved visual perception,” pp. 3227–3234, Apr. 2020.
- [32] M. Hussain, “Yolov5, yolov8 and yolov10: The go-to detectors for real-time vision,” 2024.
- [33] Zhou Wang, A. C. Bovik, H. R. Sheikh, and E. P. Simoncelli, “Image quality assessment: From error visibility to structural similarity,” *IEEE Transactions on Image Processing*, vol. 13, no. 4, pp. 600–612, Apr. 2004.
- [34] C. O. Ancuti, C. Ancuti, C. D. Vleeschouwer, and P. Bekaert, “Color balance and fusion for underwater image enhancement,” *IEEE Transactions on Image Processing*, vol. 27, no. 1, pp. 379–393, Jan. 2018.
- [35] A. Dudhane, P. Hambarde, P. Patil, and S. Murala, “Deep underwater image restoration and beyond,” *IEEE Signal Processing Letters*, vol. 27, pp. 675–679, 2020.
- [36] D. Guo, Y. Huang, T. Han, H. Zheng, Z. Gu, and B. Zheng, “Marine snow removal,” in *OCEANS*, Feb. 2022, pp. 1–7.
- [37] C. Li, S. Anwar, J. Hou, R. Cong, C. Guo, and W. Ren, “Underwater image enhancement via medium transmission-guided multi-color space embedding,” *IEEE Transactions on Image Processing*, vol. 30, pp. 4985–5000, 2021.
- [38] P. Zhuang, J. Wu, F. Porikli, and C. Li, “Underwater image enhancement with hyper-laplacian reflectance priors,” *IEEE Transactions on Image Processing*, vol. 31, pp. 5442–5455, 2022.
- [39] S. Anwar, C. Li, and F. Porikli, “Deep underwater image enhancement,” *arXiv:1807.03528*, 2018-07.
- [40] Q. Jiang, Y. Gu, C. Li, R. Cong, and F. Shao, “Underwater image enhancement quality evaluation: Benchmark dataset and objective metric,” *IEEE Transactions on Circuits and Systems for Video Technology*, vol. 32, no. 9, pp. 5959–5974, Sep. 2022.

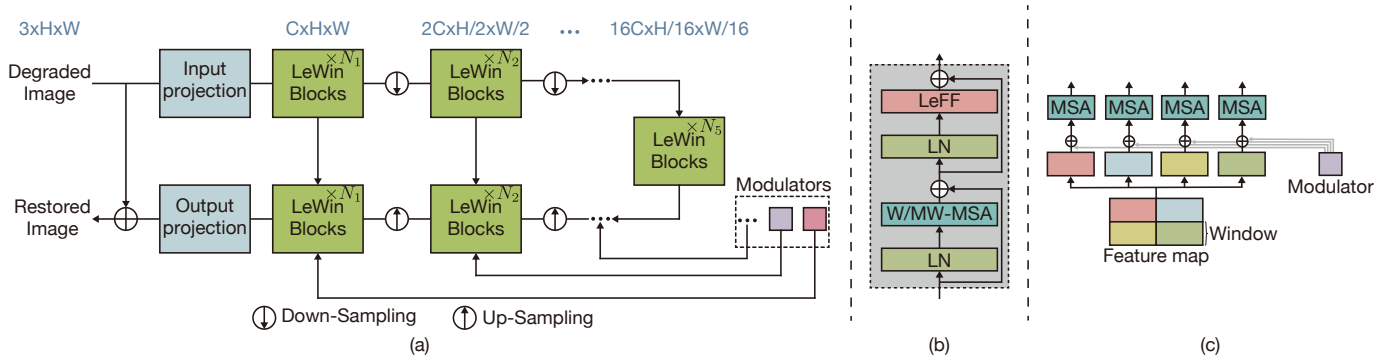


Fig. 14: (a) Uformer structure [48]. (b) LeWin block. (c) Illustration of how the modulators modulate the W-MSAs in each LeWin Transformer block (MW-MSA in (b)).

[41] S. Banerjee, G. Sanyal, S. Ghosh, R. Ray, and N. Shome, Shome, "Elimination of marine snow effect from underwater image - an adaptive probabilistic approach," in *2014 IEEE Students' Conference on Electrical, Electronics and Computer Science*, Mar. 2014, pp. 1–4.

[42] B. Cyganek and K. Gongola, "Real-time marine snow noise removal from underwater video sequences," *Journal of Electronic Imaging*, vol. 27, no. 4, p. 043002, Jul. 2018.

[43] M. Koziarski and B. Cyganek, "Marine snow removal using a fully convolutional 3d neural network combined with an adaptive median filter," in *Pattern Recognition and Information Forensics*, Dec. 2019, pp. 16–25.

[44] N. Silberman, D. Hoiem, P. Kohli, and R. Fergus, "Indoor segmentation and support inference from RGBD images," in *Computer Vision – ECCV 2012*. Springer Berlin Heidelberg, 2012, pp. 746–760.

[45] W. Wang, D. Zhu, X. Wang, Y. Hu, Y. Qiu, C. Wang, Y. Hu, A. Kapoor, and S. Scherer, "TartanAir: A dataset to push the limits of visual SLAM," *2020 IEEE/RSJ International Conference on Intelligent Robots and Systems (IROS)*, 2020.

[46] D. Akkaynak, T. Treibitz, T. Shlesinger, R. Tamir, Y. Loya, and D. Iluz, "What is the space of attenuation coefficients in underwater computer vision?" Jul. 2017, pp. 4931–4940.

[47] B. McGlamery, "Computer analysis and simulation of underwater camera system performance," *SIO ref*, vol. 75, no. 2, pp. 1–55, 1975.

[48] Z. Wang, X. Cun, J. Bao, W. Zhou, J. Liu, and H. Li, "Uformer: A general u-shaped transformer for image restoration," in *Proceedings of the IEEE/CVF Conference on Computer Vision and Pattern Recognition (CVPR)*, June 2022, pp. 17 683–17 693.

[49] J. Li, K. A. Skinner, R. M. Eustice, and M. Johnson-Roberson, "WaterGAN: Unsupervised generative network to enable real-time color correction of monocular underwater images," *IEEE Robotics and Automation Letters*, vol. 3, no. 1, pp. 387–394, Jan. 2018.

[50] D. R. Brownrigg, "The weighted median filter," *Communications of the ACM*, vol. 27, no. 8, pp. 807–818, Aug. 1984.

[51] T. Huang, G. Yang, and G. Tang, "A fast two-dimensional median filtering algorithm," *IEEE Transactions on Acoustics, Speech, and Signal Processing*, vol. 27, no. 1, pp. 13–18, Feb. 1979.

[52] F. Farhadifard, M. Radolko, and U. von Lukas, "Single image marine snow removal based on a supervised median filtering scheme," in *12th International Conference on Computer Vision Theory and Applications, VISIGRAPP 2017. Proceedings.*, vol. 4, 2017, pp. 280–287.

[53] Y. Wang, X. Yu, D. An, and Y. Wei, "Underwater image enhancement and marine snow removal for fishery based on integrated dual-channel neural network," *Computers and Electronics in Agriculture*, vol. 186, p. 106182, 2021.

[54] P. M. Moser, "Spectral transmission of light through seawater," Sep. 1992.

[55] M. Radak. (2022, Feb.) Reference air mass 1.5 spectra.

[56] J. Jiang, D. Liu, J. Gu, and S. Süsstrunk, "What is the space of spectral sensitivity functions for digital color cameras?" in *2013 IEEE Workshop on Applications of Computer Vision (WACV)*, 2013-01-01, pp. 168–179, ISSN: 1550-5790.

[57] F. Farhadifard, "Underwater image restoration: Super-resolution and deblurring via sparse representation and denoising by means of marine snow removal," *Universität Rostock*, vol. 155, 2017.

[58] E. Trucco and A. Olmos-Antillon, "Self-tuning underwater image restoration," *IEEE Journal of Oceanic Engineering*, vol. 31, no. 2, pp. 511–519, Apr. 2006.

[59] Y. Kim, H. Jung, D. Min, and K. Sohn, "Deep monocular depth estimation via integration of global and local predictions," *IEEE Trans. Image Process.*, vol. 27, no. 8, pp. 4131–4144, 2018.

[60] Y. Kim, B. Ham, C. Oh, and K. Sohn, "Structure selective depth superresolution for rgb-d cameras," *IEEE Trans. Image Process.*, vol. 25, no. 11, pp. 5227–5238, 2016.

[61] J. Cho, D. Min, Y. Kim, and K. Sohn, "Diml/cv1 rgb-d dataset: 2m rgb-d images of natural indoor and outdoor scenes," 2021.

[62] —, "Deep monocular depth estimation leveraging a large-scale outdoor stereo dataset," *Expert Systems with Applications*, vol. 178, p. 114877, 2021.

[63] S. Kim, D. Min, B. Ham, S. Kim, and K. Sohn, "Deep stereo confidence prediction for depth estimation," in *2017 IEEE Int. Conf. Image Process. ICIP*, 2017, pp. 992–996.

[64] A. Mittal, R. Soundararajan, and A. C. Bovik, "Making a "completely blind" image quality analyzer," *IEEE Signal Process. Lett.*, vol. 20, no. 3, pp. 209–212, 2013.

[65] E. Trudnowska, L. Lacour, M. Ardyna, A. Rogge, J. O. Irisson, A. M. Waite, M. Babin, and L. Stemmann, "Marine snow morphology illuminates the evolution of phytoplankton blooms and determines their subsequent vertical export," *Nature communications*, vol. 12, no. 1, p. 2816, May 2021.